

Main-sequence companions to white dwarfs – II. The age–activity–rotation relation from a sample of *Gaia* common proper motion pairs

A. Rebassa-Mansergas,^{1,2★} J. Maldonado,³ R. Raddi¹, S. Torres,^{1,2} M. Hoskin^{1,4}, T. Cunningham^{1,4},
M. A. Hollands^{1,5}, J. Ren^{1,6}, B. T. Gänsicke^{1,4}, P.-E. Tremblay⁴ and M. Camisassa¹

¹Departament de Física, Universitat Politècnica de Catalunya, c/Esteve Terrades 5, E-08860 Castelldefels, Spain

²Institute for Space Studies of Catalonia, c/Gran Capità 2–4, Edif. Nexus 104, E-08034 Barcelona, Spain

³INAF – Osservatorio Astronomico di Palermo, Piazza del Parlamento 1, I-90134 Palermo, Italy

⁴Department of Physics, University of Warwick, Coventry CV4 7AL, UK

⁵Department of Physics and Astronomy, University of Sheffield, Sheffield S3 7RH, UK

⁶CAS Key Laboratory of Space Astronomy and Technology, National Astronomical Observatories, Chinese Academy of Sciences, Beijing 100101, China

Accepted 2023 October 2. Received 2023 September 12; in original form 2023 April 28

ABSTRACT

Magnetic activity and rotation are related to the age of low-mass main-sequence stars. To further constrain these relations, we study a sample of 574 main-sequence stars members of common proper motion pairs with white dwarfs, identified thanks to *Gaia* astrometry. We use the white dwarfs as age indicators, while the activity indexes and rotational velocities are obtained from the main-sequence companions using standard procedures. We find that stars older than 5 Gyr do not display H α nor Ca II H&K emission unless they are fast rotators due to tidal locking from the presence of unseen companions and that the rotational velocities tend to decrease over time, thus supporting the so-called gyrochronology. However, we also find moderately old stars ($\simeq 2$ –6 Gyr) that are active presumably because they rotate faster than they should for their given ages. This indicates that they may be suffering from weakened magnetic braking or that they possibly evolved through wind accretion processes in the past. The activity fractions that we measure for all stars younger than 5 Gyr range between $\simeq 10$ and 40 per cent. This is line with the expectations, since our sample is composed of F, G, K, and early M stars, which are thought to have short (< 2 Gyr) activity lifetimes. Finally, we observe that the H α fractional luminosities and the R'_{HK} indexes for our sample of (slowly rotating) stars show a spread ($-4 > \log(L_{\text{H}\alpha}/L_{\text{bol}})$; $\log(R'_{\text{HK}}) > -5$) typically found in inactive M stars or weakly active/inactive F, G, K stars.

Key words: (stars:) binaries: general – stars: activity – stars: low-mass – (stars:) white dwarfs.

1 INTRODUCTION

Magnetic field generation and angular momentum evolution are of fundamental importance to understand the physical properties of low-mass main-sequence stars. These processes have been studied over several decades and the current picture can be summarized as follows.

In partially convective stars of spectral types late F, G, K, and early M, magnetic fields arise due to a combination of differential rotation and convection, the so-called Ω and α effects, respectively (Parker 1955; Leighton 1969; Spiegel & Zahn 1992; Charbonneau 2005; Browning 2008). This $\alpha - \Omega$ dynamo is thought to generate the magnetic fields at the tachocline (the transition region between the radiative and convective zones) of these stars. On the other hand, fully convective stars of spectral types later than $\simeq M3$ do not have a tachocline and are thought to rotate as rigid bodies (Barnes et al. 2005); hence, an α^2 dynamo is expected to generate the magnetic fields in these stars (Raedler et al. 1990; Chabrier & Küker 2006).

A γ^2 dynamo, based only on the turbulent cross-helicity effect, can also explain the generation of magnetic fields in fully convective stars (Pipin & Yokoi 2018).

Observationally, it has been found that for partially convective stars the efficiency of magnetic field generation, which results in higher levels of magnetic activity, is strongly correlated with the Rossby number, defined as $R_0 = P_{\text{rot}}/\tau_0$, where P_{rot} is the rotational period and τ_0 is the convective overturn timescale (Noyes et al. 1984; Garraffo et al. 2018). Thus, for a fixed τ_0 , stars that rotate faster display more signs of magnetic activity at their surfaces (Wilson 1966; Kraft 1967a; Hartmann & Noyes 1987). This connection between rotation and the efficiency of generating magnetic fields is also expected for fully convective stars (Durney & Stenflo 1972; Chabrier & Küker 2006; Shulyak et al. 2017; Wright et al. 2018), although some observational studies point out that this does not have to be necessarily the case (e.g. West & Basri 2009). In particular, Mohanty et al. (2002) and Reiners & Basri (2010) found no clear correlation between rotation and activity for ultracool M stars of spectral types M7–9.5 and Kiman et al. (2021) suggest a decreasing activity trend for M7 stars. It has to be also emphasized that, even though a faster rotation generally implies higher signs of

* E-mail: alberto.rebassa@upc.edu

magnetic activity, both the strength of the magnetic fields and the X-ray emission of the stars saturate at $R_0 \simeq 0.1$ (Pizzolato et al. 2003; Reiners, Basri & Browning 2009; Astudillo-Defru et al. 2017; Magaudda et al. 2020; Pineda, Youngblood & France 2021).

Given that low-mass main-sequence stars suffer from magnetic braking in which angular momentum is extracted from the convective envelope and lost through a magnetized wind, their rotational periods decrease in time (Skumanich 1972; Mestel 1984; Mestel & Spruit 1987; Kawaler 1988; Sills, Pinsonneault & Terndrup 2000; West et al. 2008; Meibom et al. 2015). The time-scales at which the rotational periods decrease have been observed to significantly change depending on the mass of the star. Thus, the rotational braking is considerably faster for partially convective stars than for fully convective stars (Reiners & Basri 2008; Browning et al. 2010; Schreiber et al. 2010; Zorotovic et al. 2016) and lower-mass partially convective stars spin down slower than higher-mass stars (Barnes 2003; Barnes & Kim 2010). However, it is not clear yet what physical mechanisms are behind this disruption of magnetic braking for fully convective stars. Some studies suggest a change in the magnetic field topology (Donati et al. 2008; Morin et al. 2008; Reiners & Basri 2009; Morin et al. 2010; Réville et al. 2015) or a drop in radius (Reiners & Mohanty 2012) as possible causes. Due to the strong correlation between rotation and activity, age and activity are correlated too (Houdebine et al. 2017), and it is expected that the activity lifetimes (i.e. the time a star is magnetically active) of fully convective stars are considerably longer than of partially convective stars, a hypothesis that seems to be confirmed by observations (e.g. West et al. 2008; Rebassa-Mansergas, Schreiber & Gänsicke 2013a). However, it has to be emphasized that measuring stellar ages, and hence activity lifetimes, is a difficult endeavour subject to substantial uncertainties (Soderblom 2010; Anguiano et al. 2010).

Dating low-mass main-sequence stars to study the age-activity relation relies (1) on the analysis of the Ca II H&K lines as a proxy of age (Mamajek & Hillenbrand 2008; Pace 2013), (2) on their kinematic properties (Zhao et al. 2015; Newton et al. 2016; Angus et al. 2020; Yuxi et al. 2021), (3) on asteroseismology (Metcalf et al. 2012; Chaplin et al. 2014; Silva Aguirre et al. 2017; Booth et al. 2020), (4) on using the X-ray emission as an age estimator (Mamajek & Hillenbrand 2008; Maldonado et al. 2010); (5) on the presence of lithium in the spectra to date young stars (Gutiérrez Albarrán et al. 2020); and (6) on isochrone fitting (Angus et al. 2019). Using the rotation of a given star to derive its age, the so-called gyrochronology, is also a widely used technique to estimate stellar ages (Epstein & Pinsonneault 2014; Angus et al. 2015). However, there exists evidence that stars that are halfway through their main-sequence lifetimes suffer from weakened magnetic braking and, as a consequence, are anomalously rapidly rotating (van Saders et al. 2016; Hall et al. 2021). Since only stars that are younger than 1 Gyr have been used as calibrators (Barnes 2010; García et al. 2014; Angus et al. 2015), the technique of gyrochronology should be used with caution for stars that are more evolved than the Sun, unless weakened magnetic braking is taken into account (Sadeghi Ardestani, Guillot & Morel 2017; Metcalfe et al. 2020).

To provide additional observational inputs, in this work we study the age-rotation-activity relations using binaries consisting of a low-mass main-sequence star and a white dwarf (hereafter WDMS binaries). This approach relies on measuring accurate ages from the white dwarfs. To that end one requires measuring the cooling ages and masses of the white dwarfs, which together with an initial-to-final mass relation (e.g. Catalán et al. 2008; Cummings et al. 2018; Barrientos & Chanamé 2021), allows determining the main-sequence progenitor masses and their lifetimes (Fouesneau et al. 2019; Qiu

et al. 2020; Lam et al. 2020). This alternative way of analysing the age-rotation-activity relation for low-mass main-sequence stars has been explored in the past by Morgan et al. (2012), by Skinner et al. (2017), and by our own group (Paper I; Rebassa-Mansergas et al. 2013a) via analysing WDMS binaries identified within the Sloan Digital Sky Survey (SDSS; Rebassa-Mansergas et al. 2010, 2012, 2013b, 2016a). Unfortunately, despite being the most numerous and homogeneous sample of (spectroscopic) WDMS binaries, the SDSS catalogue suffers from important selection effects (Rebassa-Mansergas et al. 2010). For instance, white dwarfs cooler than $\simeq 10\,000$ K are clearly underrepresented. This effect considerably reduces the range of studied white dwarf cooling times and biases the sample against larger ages. Moreover, the main-sequence companions are typically M dwarfs, which implies F, G, and K stars cannot be analysed and therefore assigned an age. The motivation of the study presented here is to surpass these limitations by analysing a sample of WDMS binaries in common proper motion pairs (CPMPs), identified thanks to *Gaia* astrometry. Since the two stars are widely separated they are expected to have evolved avoiding mass transfer episodes. However, it is possible that the main-sequence companions may have accreted material from the white dwarf progenitors via stellar winds, thus gaining angular momentum (Jeffries & Stevens 1996; Boffin 2015), which may alter the expected age-rotation-activity relations (Zurlo et al. 2013; Leiner et al. 2018; Bowler et al. 2021; Gratton et al. 2021). In any case, they can be independently observed, which allows targeting both cooler white dwarfs and higher mass main-sequence stars.

2 THE WDMS BINARY SAMPLE

In Rebassa-Mansergas et al. (2021), we provided a catalogue of 4415 common proper motion pairs (CPMPs) formed by a white dwarf and a main-sequence star, identified within the second data release of *Gaia* (Gaia Collaboration et al. 2018). We also performed high-resolution spectroscopic observations¹ of 235 main-sequence companions to derive their [Fe/H] abundances, which together with the total ages derived from the white dwarf primaries allowed us to constrain the age-metallicity relation in the solar neighbourhood. Given that the primary aim of that work was to measure the [Fe/H] abundances of the companions, our follow-up observations focused on F, G, K, and early-type M dwarfs, thus excluding M dwarfs of effective temperatures under $\simeq 3000$ K for which it becomes extremely challenging to derive metallicities. Thus, the present sample of observed targets clearly lacks objects containing fully convective (intrinsically fainter) companions and comprises objects that are brighter and closer to the Sun as compared to the entire catalogue of 4415 CPMPs (see Fig. 1). To this sample of 235 WDMS CPMPs, we add in this work 427 pairs that were either part of our follow-up high-resolution observations but have no [Fe/H] abundance determinations due to the lack of convergence in the fits (115 objects) or had available low/medium resolution spectra from LAMOST (Large Area Multi-Object Spectroscopic Telescope; Cui et al. 2012) data release 8 (312 objects). Thus, our total initial sample of study in this work consisted of 662 WDMS CPMPs for which the main-sequence companions have available spectra obtained from our high-resolution spectroscopic follow-up observations and/or from LAMOST DR8.

¹We used the Mercator, Telescopio Nazionale Galileo and Xinglong 2.16m telescopes, see Rebassa-Mansergas et al. (2021) for details on the observations and their data reduction.

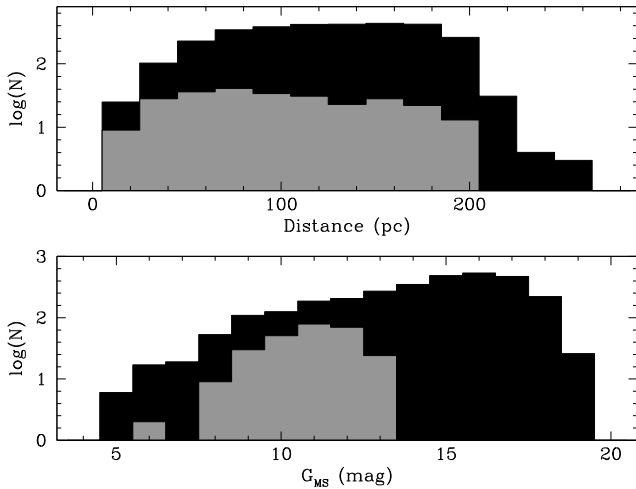


Figure 1. Distance and main-sequence star *Gaia* G magnitude for the entire sample of CPMPs from Rebassa-Mansergas et al. (2021) (black) and for those that were followed-up for high-resolution observations (grey).

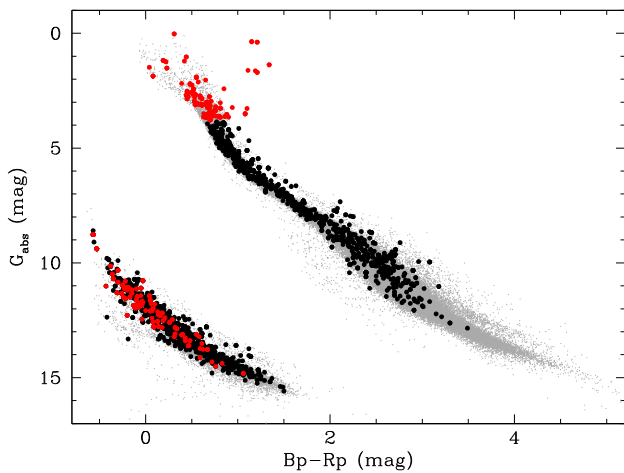


Figure 2. *Gaia* G_{abs} versus $Bp-Rp$ diagram for single white dwarfs and main-sequence stars within 100 pc (grey dots), for our initial WDMS CPMP sample (red plus black solid dots) and for our final sample to be analysed in this work (black solid dots) after excluding 85 giant stars and main-sequence stars above the Kraft break (red solid dots).

The *Gaia* M_G versus $Bp-Rp$ diagram for these targets is illustrated in Fig. 2. Inspection of the figure reveals that a few giant stars are included in our sample, and also the presence of stars above the Kraft break (i.e. the limit of outer convective envelope and occurrence of

significant chromospheric activity; Kraft 1967b), which corresponds to an effective temperature of $\simeq 6200$ K, or $M_G \simeq 3.8$ mag (Pecaut & Mamajek 2013). Therefore, we excluded these 85 giant and hot main-sequence stars by simply considering companions with $M_G < 3.8$ mag, thus reducing our total sample to 574 CPMPs (see Table 1). The coordinates of the 574 objects, the telescope used in each case and the parameters obtained throughout this work are provided in a supplementary table, available in the online version of the paper.

2.1 Orbital separations

As we have already mentioned in the introduction, the possibility exists that the progenitors of the white dwarfs in our selected WDMS binaries transferred material to the secondary stars via stellar winds in the past, when the orbital separations were shorter. This could have increased the rotation of the current main-sequence companions to the white dwarfs, therefore affecting the expected age–rotation–activity relations (Zurlo et al. 2013; Leiner et al. 2018; Bowler et al. 2021; Gratton et al. 2021). To explore this possibility, we estimated the projected orbital separations of our 574 CPMPs from their *Gaia* positions, which are shown in the top-left panel of Fig. 3. Assuming that the orbits adiabatically expanded by a maximum factor of $M_{\text{prog}}/M_{\text{WD}}$ (Jeans 1924) – where M_{WD} is the white dwarf mass and M_{prog} its progenitor mass – we expect minimum initial orbital separations 2–5 times shorter (depending on the white dwarf mass) than the current ones, according to typical initial-to-final mass relations (e.g. Catalán et al. 2008; Cummings et al. 2018). Given that there is a non-negligible fraction of systems with current orbital separations up to $\simeq 1000$ au, we conclude it is likely that a fraction ($\simeq 2$ –8 per cent) of WDMS binaries in our sample may have suffered from wind accretion episodes in the past.

2.2 Total ages

Given that not all the white dwarfs in our sample of study have available spectra, we derived the total ages in a homogeneous way from their *Gaia* photometry. The ages of the 235 DR2 WDMS CPMPs with available $[\text{Fe}/\text{H}]$ abundances from the companions were already derived by Rebassa-Mansergas et al. (2021). The method used basically interpolates the white dwarf *Gaia* G absolute magnitudes and $Bp-Rp$ colours in the evolutionary sequences of the La Plata group (Althaus et al. 2015; Renedo et al. 2010; Camisassa et al. 2016, 2019) at the corresponding metallicity (or $[\text{Fe}/\text{H}]$ abundance) to derive both the white dwarf cooling ages and their main-sequence progenitor lifetimes. This approach of deriving total ages as the white dwarf cooling plus main-sequence progenitor lifetime was tested by e.g. García-Berro et al. (2013), Torres et al. (2015), and Qiu et al. (2021), who derived the total ages of white

Table 1. In this table, we provide the number of WDMS binaries that are part of the full sample, and that are part of subsamples with available white dwarf total ages, with available main-sequence rotational velocities, with available main-sequence $H\alpha$ fractional luminosities and with available R'_{HK} indexes. For each subsample, we also indicate the number of objects that pass the cuts we implemented (age uncertainties under 1 Gyr, $v_{\text{rot}}\sin i$ errors below 1 km s^{-1} and $\log(L_{\text{H}\alpha}/L_{\text{bol}})$ uncertainties lower than 0.75) and of those, which ones are formed by M dwarfs (effective temperatures lower or equal than 3800 K and associated with errors lower than 120 K) or by FGK stars (effective temperature higher than 3800 K and associated with errors lower than 120 K). The coordinates and parameters derived in this work for each object are given in a supplementary material table.

	Full sample	Sample with ages	Sample with $v_{\text{rot}}\sin i$	Sample with $L_{\text{H}\alpha}/L_{\text{bol}}$	Sample with R'_{HK} index
Total number	574	431	195	527	111
Pass cut	515	201	102	340	111
Are M dwarfs	201	76	0	127	19
Are FGK stars	314	125	102	213	92

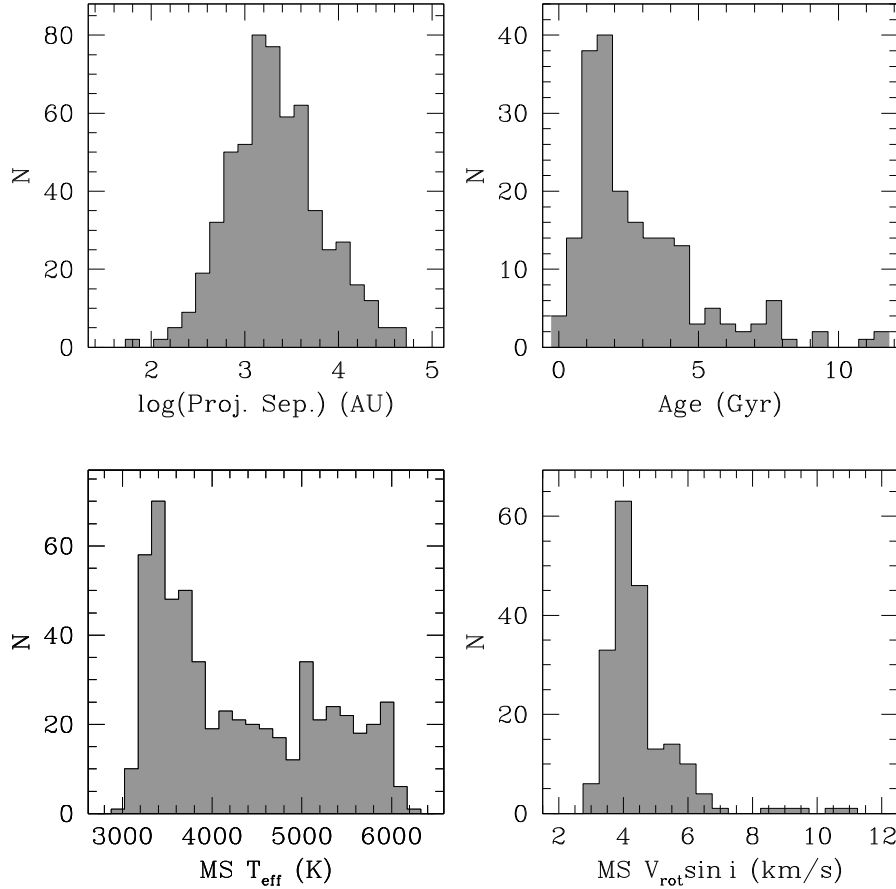


Figure 3. Distribution of projected orbital separations (top-left), ages (top-right; displaying only those values with errors less than 1 Gyr), main-sequence effective temperatures (bottom-left), and rotational velocities (bottom-right; when available).

dwarfs in open and globular clusters and found them to be consistent to those obtained from the main-sequence turn-off of the clusters. Moreover, using double white dwarfs or triple systems containing at least two white dwarfs, Heintz et al. (2022) report that total white dwarf ages are generally reliable, especially for those with masses above $0.63 M_{\odot}$. This is in line with the results of Fouesneau et al. (2019) and Moss et al. (2022), who calculated white dwarf total ages in the same way as in this work and found them to be $\simeq 5$ – 20 per cent precise. Unfortunately, this does not take into account possible uncertainties due to the initial-to-final mass relation, which may introduce differences ranging from $\simeq 0.2$ to $\simeq 2$ Gyr (see fig. 2 of Rebassa-Mansergas et al. 2016b). To avoid this issue a sample of high-mass white dwarfs in which the progenitor lifetime is considerably shorter than the cooling age is required.

In Rebassa-Mansergas et al. (2021), we assumed that all white dwarfs had hydrogen-rich atmospheres (DA white dwarfs) and we took extinction into account using the 3D *Stilism* maps of Lallement et al. (2014) and Capitanio et al. (2017). Here, we used the same method to derive the ages with the difference that we searched for available spectral types of the white dwarfs in our sample. The spectral types were adopted as hydrogen rich if the probability to be a DA measured from Jiménez-Esteban et al. (2023) for white dwarfs within 100 pc was larger than 0.5. For those with a probability under 0.5, we adopted the classification based on a random forest algorithm from García-Zamora, Torres & Rebassa-Mansergas (2023), which was developed to classify these (non-DA) systems within 100 pc into DBs, DCs, DQs, and DZs. We complemented the search, especially

for white dwarfs with distances above 100 pc, using the Montreal White Dwarf Database (Dufour et al. 2017). Thus, our sample comprises 220 DAs, 15 DBs, 58 DCs, 9 DQs, 4 DZs, and 268 unclassified white dwarfs. We have employed the hydrogen-rich evolutionary models of Camisassa et al. (2016, 2019) for DA white dwarfs and all DC white dwarfs with $B_p - R_p$ colours larger than 0.8 mag (which corresponds to effective temperatures under $\simeq 5000$ K), the pure helium-atmosphere evolutionary models of Camisassa et al. (2017) for DB white dwarfs, and the white dwarf models with helium-atmospheres and carbon traces² that follow the so-called carbon sequence enrichment of Camisassa et al. (2023) for DQ white dwarfs and for all DC white dwarfs with $B_p - R_p < 0.8$ mag. No ages were calculated for those white dwarfs with DZ spectral types. White dwarfs with no classification were considered to be hydrogen-rich. There is a possibility that non-DAs exist among the 268 unclassified objects. They have $B_p - R_p$ colours between $\simeq -0.3$ and $\simeq 0.9$ mag, which correspond to effective temperatures between $\simeq 20\,000$ and $\simeq 5\,000$ K for both hydrogen-rich and hydrogen-deficient white dwarfs according to the cooling sequences. The fraction of non-DA white dwarfs goes from $\simeq 10$ per cent at $20\,000$ K to $\simeq 25$ – 35 per cent at $10\,000$ – $5\,000$ K (McCleery et al. 2020; López-Sanjuan et al. 2022; Torres et al. 2023). Taking these values into consideration, we estimate that around 30 per cent of the unclassified

²Note that the carbon traces are not visible in the optical but are expected at ultraviolet wavelengths.

objects ($\simeq 85$) are probably non-DAs. According to Camisassa et al. (2017), cooling age differences between hydrogen-rich and helium-rich white dwarfs are lower than 0.2 Gyr, with hydrogen-rich white dwarfs being younger for a given effective temperature. The age discrepancy may be further accentuated since the derived white dwarf masses slightly vary when using hydrogen-rich and helium-rich models, which implies the progenitor lifetimes change too. If the white dwarfs are of low-mass, the total age discrepancies can be as high as 5–6 Gyr. This is the case when using DQ models too.

It has to be emphasized that the evolutionary sequences we have used do not provide total ages for white dwarfs that are less massive than $\simeq 0.5 M_{\odot}$, since the progenitors of these objects require ages longer than the Hubble time to evolve out of the main sequence and in this case the use of an initial-to-final mass relation is not appropriate. Thus, for 432 of the 574 objects we managed to derive an age and, among these, 201 have age uncertainties of less than 1 Gyr. Since the main motivation of this work is to constrain the age–rotation–activity relation, we only considered the ages of these 201 objects in our analysis. Note that of these 201, 85 have no white dwarf type classification, therefore we expect the ages of $\simeq 30$ per cent of those ($\simeq 25$ objects; i.e. $\simeq 12$ per cent of the full sample with ages) not to be fully reliable, as stated above. The resulting age distribution is illustrated in the top-right panel of Fig. 3, where it can be seen that most of the systems have ages concentrated in the 1–4 Gyr bins.

Finally, it is also important to note that for the objects that were not studied in Rebassa–ansergas et al. (2021) we adopted a solar abundance for the age calculation since the metallicities in these cases were not known. According to the white dwarf evolutionary models used in this work, which employ the progenitor lifetimes of Miller Bertolami (2016),³ this assumption may imply progenitor lifetime (hence total age) differences respect to those obtained assuming the solar metallicity value of up to $\simeq 1.5$ Gyr for low-mass white dwarfs ($\simeq 0.55 M_{\odot}$), with the average difference being 0.15 ± 0.4 Gyr over the entire white dwarf mass range. However, note that only 14 of the 201 white dwarfs with age determinations considered in this work have masses below $0.57 M_{\odot}$ and, as a consequence, we do not expect this issue to considerably affect our results. Regarding the total age errors, these were obtained directly from considering the parallax (hence absolute magnitude) and Bp–Rp uncertainties.

2.3 Main-sequence star effective temperatures

The main-sequence stars in our CPMPs were observed by a wide number of different telescopes and spectroscopic resolutions, and the spectra were subject to different signal-to-noise ratios. As a consequence, in order to acquire an as homogeneous as possible compilation, we used the *Gaia* photometry of each star rather than their corresponding spectra to derive their effective temperatures. We independently interpolated the extinction corrected G absolute magnitudes and the Bp–Rp colours in the updated tables of Pecaut & Mamajek (2013)⁴ to derive two effective temperature values for each star, which were then averaged to get a single measurement (the error was considered as the standard deviation). The corresponding distribution is provided in the bottom-left panel of Fig. 3. As expected, no

main-sequence stars can be found with effective temperatures higher than $\simeq 6200$ K, which corresponds to the Kraft break, since these objects were excluded from our sample. Moreover, the majority of stars have effective temperatures above 3000 K, as a consequence of our high-resolution follow-up observations prioritizing F, G, K, and early M dwarf companions.

2.4 Main-sequence star rotational velocities

The Mercator, TNG, and Xinglong spectra we obtained (Rebassa–Mansergas et al. 2021) are of sufficient resolution to derive projected rotational velocities. To that end we used the Fourier transform (FT) technique (e.g. Gray 2008). Following Maldonado et al. (2022), we used three spectral lines at 6335.33 Å, 6380.75 Å, and 6393.61 Å for the computations. The values obtained from the different lines were averaged into a single measurement, while the standard deviation was considered as the associated uncertainty. The dominant term in the FT of the rotational profile is a first-order Bessel function that produces a series of relative minima at regularly spaced frequencies. The first zero of the FT and the projected rotational velocity are related by

$$v_{\text{rot}} \sin i = \frac{c}{\lambda} \times \frac{k_1}{\sigma_1}, \quad (1)$$

where λ is the central wavelength of the considered line, c is the speed of light, σ_1 is the position of the first zero of the FT, and k_1 is a function of the limb darkening coefficient (ϵ). The term k_1 can be approximated by a fourth-order polynomial degree (Dravins, Lindgren & Torkelsson 1990)

$$k_1 = 0.610 + 0.062\epsilon + 0.027\epsilon^2 + 0.012\epsilon^3 + 0.004\epsilon^4, \quad (2)$$

where we assume $\epsilon = 0.6$ (see e.g. Gray 2008).

We managed to derive projected rotational velocities for 195 stars and the corresponding distribution is provided in the bottom-right panel of Fig. 3. It reveals that the vast majority of the main-sequence stars in our sample are apparently slow rotators ($V_{\text{rot}} \sin i < 6 \text{ km s}^{-1}$) and that the minimum detectable value is $\simeq 3 \text{ km s}^{-1}$. The typical errors are between 0.1 and 2 km s^{-1} with an average value of $\simeq 1.2 \pm 1 \text{ km s}^{-1}$, independently of the spectrograph used.

2.5 Main-sequence star radial velocities

Emission lines (e.g. H α) due to magnetic activity may arise not only for main-sequence stars that are young in our sample, but also if they are in close orbits with unseen companions and therefore forced to rotate fast due to tidal locking. If that was the case, we would detect radial velocity variations.

We derived the radial velocities from the TNG, Mercator, Xinglong, and LAMOST medium resolution spectra of the main-sequence stars in an homogeneous way following Rebassa–Mansergas et al. (2007): we fitted the H α emission/absorption with a single Gaussian plus a parabola. H α is the only suitable line sampled by the spectra obtained from all telescopes. For 287 of the 574 systems in our sample we measured at least one radial velocity; for 107 two or more. For 105, the available velocities come from spectra separated by at least one night. We detected more than 3σ radial velocity variation in 7 systems ($\simeq 6$ per cent of the sample with more than one velocity). For the 107 objects with more than one measurement, we show in Fig. 4 the absolute value of the radial velocity difference as a function of the absolute value of the time difference between the heliocentric Julian date of the minimum and maximum velocities.

³These main-sequence lifetimes are consistent to those of Pietrinferni et al. (2004) and the theoretical initial-to-final mass relation employed is remarkably similar to the one by Catalán et al. (2008) for $Z = 0.02$ and similar to the one by Cummings et al. (2018) for $Z = 0.001$.

⁴https://www.pas.rochester.edu/~emamajek/EEM_dwarf_UBVIJHK_colors_Teff.txt

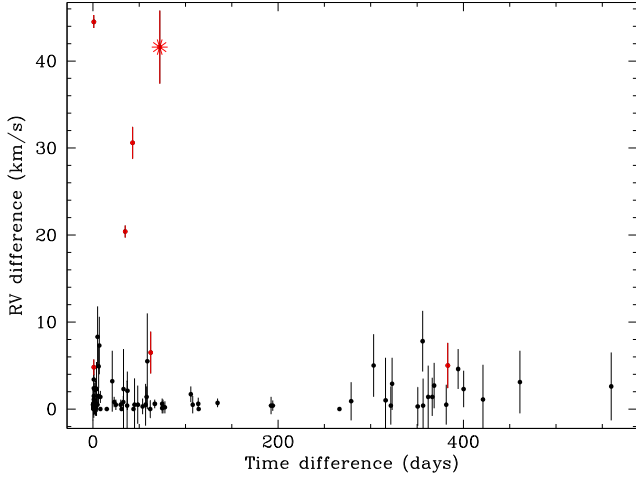


Figure 4. The absolute value of the radial velocity difference as a function of the absolute value of the difference between the heliocentric Julian dates corresponding to the maximum and minimum radial velocities. Red solid dots indicate the seven stars displaying more than 3σ radial velocity variation. The red star indicates this object displays H α in emission.

The seven stars displaying more than 3σ variation are shown in red in Fig. 4. These are J0227 + 6355, J0309 + 3340, J0314 + 3248, J0708 + 7831, J0804 + 1207, J1514 + 0157, and J1559 + 2528. Only J0708 + 7831, associated with a time difference of 72 d, displays H α in emission (none display Ca II H&K emission). We do not derive a reliable age for this object (Section 2.2); therefore, the emission might be a simple consequence of the star being young. The current projected orbital separation is estimated as 1991 au, indicating that it is unlikely that wind accretion took place in the past. The remaining 6 objects display H α in absorption and are all G and K dwarfs with projected orbital separations above 1600 au, with the exception of J1514 + 0157 which has a separation of 680 au. Except perhaps for J1514 + 0157, the radial velocity variations might arise due to the presence of hidden, nearby and less luminous M dwarf companions. That is, they are candidates for being hierarchical triple systems composed of an inner unresolved main-sequence binary and an outer white dwarf. Note that this is also a possibility for J0708 + 7831, which displays H α in emission.

2.6 Activity indicators

We used two activity indicators to evaluate whether the main-sequence stars in our WDMS CPMPs are magnetically active or not. The first was the presence of H α emission, through the measurement of the equivalent width of the line. The second was the presence of Ca II H&K emission, via the analysis of the S_{HK} index.

We measured the H α equivalent width ($\text{EW}_{\text{H}\alpha}$) following the method described in Paper I. That is, we first fitted the flux in the 6420–6700 Å range with a parabola. The fit, which excluded the H α $-7 < \lambda < \text{H}\alpha + 7$ Å region, was then used to normalize the spectra. The $\text{EW}_{\text{H}\alpha}$ was measured from the normalized spectra within the H α $-7 < \lambda < \text{H}\alpha + 7$ Å region and active stars were identified from the following criteria:

$$\text{SNR} \geq 10, \quad (3)$$

$$\text{EW}_{\text{H}\alpha} \leq -0.75 \text{ \AA}, \quad (4)$$

$$|\text{EW}_{\text{H}\alpha}| > 3 \times |\text{eEW}_{\text{H}\alpha}|, \quad (5)$$

$$h > 3 \times N_{\text{cont}}, \quad (6)$$

where SNR is the signal-to-noise ratio of the spectra, the $\text{EW}_{\text{H}\alpha}$ error is $\text{eEW}_{\text{H}\alpha}$, h is the peak of the flux at H α above the continuum, and N_{cont} is the noise at continuum level (see an example in Fig. 5, middle left panel). We flagged as inactive stars those fulfilling equation 1 and the inverted forms of equations (2)–(4) (see an example in Fig. 5, top left panel). Those stars that did not pass the active or inactive criteria (mainly due to the low SNR of their spectra) were not given an activity index.

Main-sequence stars with more than one available spectrum were considered inactive when no emission was detected in any of the spectra. Thus, the above exercise resulted in 33 active and 525 inactive stars according to the detection of H α emission. The remaining 16 objects had all their spectra of SNR under 10 and we hence decided not provide any activity classification. Visual inspection of the spectra revealed that only $\simeq 3$ per cent of the sample was misclassified. In particular, 17 spectra were flagged as inactive whilst visual inspection revealed mild H α emission (see an example in Fig. 5, bottom left panel).

The S_{HK} index is our second activity indicator, especially useful for F, G, and K (hereafter FGK) stars since it is based on the Ca II H&K doublet. It is defined as follows (Wilson 1968, 1978; Vaughan, Preston & Wilson 1978; Duncan et al. 1991; Baliunas et al. 1995):

$$S_{\text{HK}} = \beta \frac{H + K}{R + V}, \quad (7)$$

where H and K are the integrated fluxes (or number of counts if the spectra are not flux-calibrated) within 2 \AA rectangular windows around the Ca II H ($3968.47 \pm 1 \text{ \AA}$) and Ca II K ($3933.66 \pm 1 \text{ \AA}$) lines, respectively; R and V are the integrated fluxes (or number of counts) within 20 \AA rectangular windows (i.e. continuum windows) to the right ($3991\text{--}4011 \text{ \AA}$) and left ($3891\text{--}3911 \text{ \AA}$) sides of the H&K lines, respectively, and β is calibration constant. The choice of 2 \AA rectangular boxes for obtaining H and K follows Zhao et al. (2011), which implies $\beta = 10$ since the continuum windows are 10 times wider than the H&K windows. To measure H, K, R, and V, the spectra were previously normalized. We considered first the sum of the fluxes at ten continuum ranges (defined as $3881 \pm 1 \text{ \AA}$, $3891 \pm 1 \text{ \AA}$, $3901 \pm 1 \text{ \AA}$, $3911 \pm 1 \text{ \AA}$, $3956 \pm 1 \text{ \AA}$, $3981 \pm 1 \text{ \AA}$, $3991 \pm 1 \text{ \AA}$, $4001 \pm 1 \text{ \AA}$, $4011 \pm 1 \text{ \AA}$, and $4021 \pm 1 \text{ \AA}$) and fitted then these fluxes with a second-order polynomial, which was used to normalize the spectra.

It has to be emphasized that the S_{HK} index obtained here should not be directly compared to that from the original survey definition (Wilson 1968) since they employed triangular rather than rectangular H&K windows (although this effect is expected to be minor, see Hall, Lockwood & Skiff 2007) and also because the β constant is different. However, it perfectly serves our purpose as an activity indicator. In this sense, we selected all stars with an S_{HK} value greater (smaller) than 0.75 as active (inactive) stars (see examples in the middle and top right panels of Fig. 5, respectively). This threshold was obtained by analysing the S_{HK} indexes of those stars that are active or inactive based on the H α emission of their spectra and resulted in 29 active and 157 inactive stars. Note that the number of stars with activity indicators provided by the S_{HK} index is smaller than that with H α emission indicators because (1) the LAMOST medium resolution spectra do not cover the Ca II H&K lines and (2) for several stars, especially M dwarfs, the Ca II H&K lines were too noisy. Visual inspection of the spectra revealed that in $\simeq 6$ per cent of the cases the above exercise resulted in wrong classifications. In particular, 17 spectra with S_{HK} index below 0.75 turned out to be active, 12 from

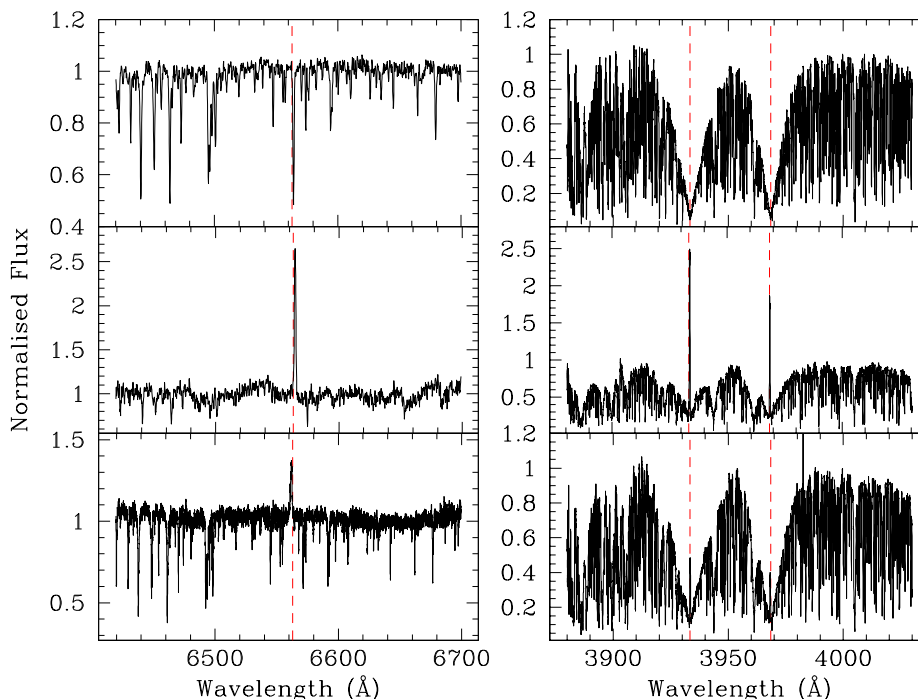


Figure 5. Left-hand panels: example spectra of inactive (top; spectrum of J1217+3423 obtained by LAMOST with the medium resolution instrument), active (middle; spectrum of J0001+3559 obtained by LAMOST with the medium resolution instrument) and weakly active (bottom; J1014+6155, considered as active after visual inspection, obtained by the TNG, Telescopio Nazionale Galileo, with the HARPS-N spectrograph) objects based on the presence or lack of H α emission. Right panels: example spectra (all obtained with the Mercator telescope equipped with the HERMES spectrograph) of inactive (top; J2328 + 1045), active (middle; J0221 + 5333) and weakly active (bottom; J0209 – 0140, considered as active after visual inspection) objects based on the presence or lack of Ca II H&K emission. The dashed red vertical lines indicate the position of the H α and Ca II H&K lines.

observed by the TNG/HARPS-N and 5 by the Mercator/HERMES telescope/spectrograph. These two configurations yield very high resolution spectra ($R = 115\,000$ and $85\,000$, respectively), which allows visually detecting weak chromospheric H&K emission (see an example in the bottom right panel of Fig. 5).

After the above exercises, we combined the H α and S_{HK} indicators to give a final activity flag to our stars. That is, if the two indicators are available we considered a star as inactive if both classifications are inactive. A star was considered as active if at least one of the indicators classified the star as active. Thus, the final number of active/inactive stars in our sample is 49/509, i.e. an overall fraction of active stars of ≈ 10 per cent (see Section 3 for further discussions).

3 FRACTION OF ACTIVE STARS

We represent the fraction of active stars as a function of age in Fig. 6. The top-left panel illustrates the fractions for the whole sample, i.e. stars with activity indexes available and with ages associated with uncertainties under 1 Gyr. The top-right panel shows the same but considering only objects that were observed with high-resolution spectrographs, which allow detecting weaker emission lines. The comparison reveals that, as expected, the activity fractions overall increase when we consider high-resolution spectra, but the pattern remains the same. In particular, the highest activity fraction corresponds to the younger bin and no stars displaying H α nor Ca II H&K emission in their spectra are found older than 5 Gyr. The exception is J1634 + 5710, which turned out to be the well-known eclipsing main-sequence binary CM Dra (implying this is a hierarchical triple system formed by an inner main-sequence binary

and an outer DQ white dwarf companion) with an orbital period of 1.27 d (Lacy 1977; Metcalfe et al. 1996; Morales et al. 2009) and an age of 8.5 ± 3.5 Gyr (Feiden & Chaboyer 2014), in agreement with our age derivation of 6.8 ± 0.4 Gyr from the DQ white dwarf. In this case, activity is enhanced due to the fast rotation of the M star rather than by it being young. The lack of systems displaying emission lines above 5 Gyr is consistent with an upper limit to the probability that a star is active of 2 per cent, within 1σ . Even though the number of such old stars is only 25, this is a confirmation that young stars are generally more active presumably because they rotate faster and that relatively old stars do not appear to be magnetically active since they have been further exposed to magnetic braking (with the exception of stars that are members of close binaries). As expected, the activity fractions gradually decrease until 3 Gyr, however at this point they increase back, which is at odds with the idea that stars become less active as they grow old. This feature can be understood as follows.

Given that the lifetime of a main-sequence star depends on its mass (or effective temperature), with increasing lifetimes for decreasing masses (Tuffs et al. 2004, see their equations A.10), the spread of ages at a given effective temperature increases with decreasing effective temperature. Thus, between 0.1 and 5 Gyr our sample is a mix of stars at different effective temperatures, T_{eff} , but with a clear concentration of hotter objects ($T_{\text{eff}} \gtrsim 5000$ K) at younger ages ($\lesssim 2$ Gyr; see the bottom panels of Fig. 6). Since the activity lifetimes are also a function of mass, with massive (and hotter) stars having considerably lower activity lifetimes (West et al. 2008; Reiners & Mohanty 2012), the activity fractions abruptly decrease for ages in the range of ≈ 0.1 –3 Gyr. The fact that hotter stars ($T_{\text{eff}} \gtrsim 5000$ K) are less common after ≈ 4 –5 Gyr, combined with the longer activity

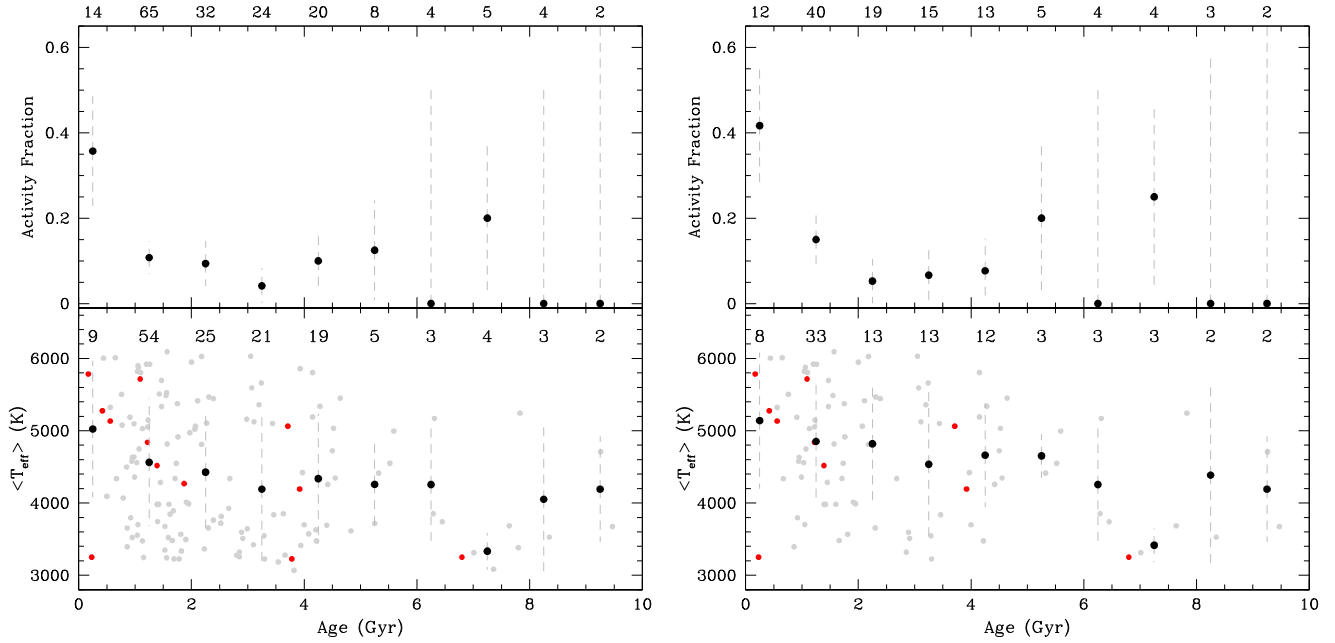


Figure 6. Top panels: Activity fractions as a function of age for the entire sample of main-sequence companions to white dwarfs studied in this work (left panel) and for those stars that we observed with high-resolution spectrographs (right). The number of stars in each bin are indicated on the top of the panels. Bottom panels: the distribution of effective temperatures per age bin (grey dots; red dots indicate active stars) together with the associated mean and standard deviations (black solid dots and lines, respectively). The number of stars per age bin are also indicated in the top. Note that not all stars with derived ages have measured effective temperatures with uncertainties under 120 K.

lifetimes of cooler stars, implies that the activity fractions increase back between $\simeq 3$ and 5 Gyr.

To further investigate the relation between effective temperature and activity we show in Fig. 7 the activity fractions as a function of effective temperature. The top-left panel displays the fractions for the whole sample (stars with activity indexes available and with effective temperature uncertainties under 120 K) and the top-right panel the fraction for those stars that were observed with higher resolution spectrographs. The values are similar except for the coolest bin, where the percentage of stars that are active increases considerably from $\simeq 0.1$ to $\simeq 0.5$. Even though the number of stars associated to high-resolution spectra at this bin ($\simeq 3000$ K) is very low, this increase is not unexpected since we are near the fully convective boundary (Baraffe & Chabrier 2018), and fully convective stars have considerably higher activity lifetimes (Rebassa-Mansergas et al. 2013a). The fluctuations in the activity fractions between 3000 and 6000 K are a consequence of the stars having different combinations of ages in each bin (see the bottom panels of Fig. 7).

4 THE ROTATION-ACTIVITY RELATION

In this section, we first study the rotation-activity relation for our sample of stars with measured projected rotational velocities ($V_{\text{rot}} \sin i$) and H α equivalent widths. Then, we study the same relation for those stars with measured rotational velocities and available S_{HK} indexes.

The strength of magnetic activity was quantified as the logarithm of the ratio between the H α luminosity and the bolometric luminosity, i.e. $\log(L_{\text{H}\alpha}/L_{\text{bol}})$, which was obtained as

$$L_{\text{H}\alpha}/L_{\text{bol}} = \chi \times |\text{EW}_{\text{H}\alpha}|, \quad (8)$$

where $\text{EW}_{\text{H}\alpha}$ is the H α equivalent width and χ is the ratio between the continuum flux near the H α line and the bolometric flux at a given effective temperature. In this exercise, we adopted the χ values provided by Fang et al. (2018), which are defined for a wide range of effective temperatures (from 2800 to 6800 K). Moreover, the rotational velocities considered had errors of less than 1 km s^{-1} and the $\log(L_{\text{H}\alpha}/L_{\text{bol}})$ values were restricted to errors no larger than 0.75. It is important to emphasize that, previous to the mentioned calculations, the $\text{EW}_{\text{H}\alpha}$ measurements were corrected from basal values of inactive stars following Fang et al. (2016). In particular, we fitted a third-order polynomial to the $\text{EW}_{\text{H}\alpha}$ of inactive stars in our sample and the results from the fit were subtracted so that the corrected $\text{EW}_{\text{H}\alpha}$ values were either zero or lower than that.

The results obtained are illustrated in the top panel of Fig. 8 and encompass the $L_{\text{H}\alpha}/L_{\text{bol}}$ versus rotation relation for 43 FGK stars. For comparison, we also include in this figure the relation we obtained in Paper I for 47 M dwarfs in tight binaries with white dwarfs (blue solid dots; note that in this case the orbital periods were known and, as a consequence, the rotational velocities were not affected by the $\sin i$ factor) and the results by Reiners, Joshi & Goldman (2012) for 242 single M dwarfs with measured projected rotational velocities.

Whilst the sample studied in Paper I populates the regime in which the strength of magnetic activity saturates, i.e. $\log(L_{\text{H}\alpha}/L_{\text{bol}}) \sim -3.5$ independently of rotation, most of the stars analysed in this work are located in the area expected for inactive or weakly active stars ($L_{\text{H}\alpha}/L_{\text{bol}} < -4$), typical of slower rotators. Indeed, none of the 43 FGK stars display H α in emission. Given that the full sample of stars considered in this exercise have FGK spectral types, it is not entirely surprising that in some cases the strength of magnetic activity reached values higher than -4 . In FGK stars the H α line is generally found in absorption and the depth of the line decreases as soon as the level of magnetic activity increases. In other words, the H α line is radiation-

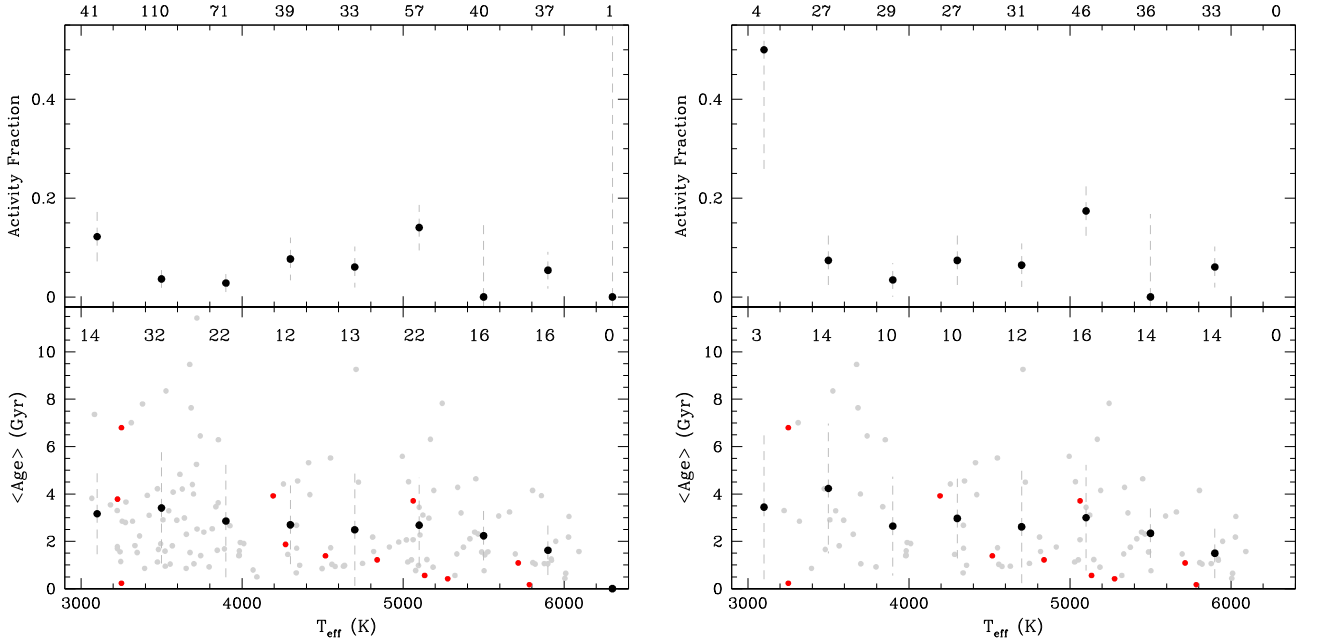


Figure 7. Top panels: Activity fractions as a function of effective temperatures for the entire sample of main-sequence companions to white dwarfs studied in this work (left panel) and for those stars that we observed with high-resolution spectrographs (right). The number of stars in each bin are indicated on the top of the panels. Bottom panels: The distribution of ages per temperature bin (grey dots; red dots indicate active stars) together with the associated mean and standard deviations (black solid dots and lines, respectively). The number of stars per age bin are also indicated in the top. Note that not all stars with derived effective temperatures have measured ages.

dominated, i.e. the increase of the optical depth initially leads to a deeper absorption profile, until the electron density is high enough to take the line into the collisionally dominated formation regime.⁵ Only in those cases in which the level of magnetic activity is very high the line will be seen in emission. As a consequence, weakly active FGK stars will not display emission, but less absorption than inactive stars. This implies that after applying the basal correction to the measured $EW_{H\alpha}$, the corrected values will be negative for those that are weakly active. Thus, the more active the star, the more negative the corrected $EW_{H\alpha}$ and the higher the $L_{H\alpha}/L_{bol}$ value. We conclude that the results provided by Paper I and this work clearly support the idea that the strength of magnetic activity gradually increases for increasing rotation and that it saturates when the rotational velocities of the stars are higher than $\simeq 10 \text{ km s}^{-1}$.

To quantify the level of chromospheric Ca II H&K emission, we derived the R'_{HK} index as introduced by Noyes et al. (1984, see the Appendix), which is defined as $R'_{HK} = R_{HK} - R_{phot}$ (see also Hall et al. 2007; Lovis et al. 2011; Mittag, Schmitt & Schröder 2013). R_{phot} is the photospheric contribution, which depends on the $(B - V)$ colour of the star. R_{HK} gives the emission normalized to the bolometric brightness of the star and it also depends on its $(B - V)$ colour as well as on the S_{HK} index on the Mount Wilson scale. Since the S_{HK} values we obtained in Section 2.6 are not in the required scale and no stars in our sample have available Mount Wilson S_{HK} indexes in the literature (e.g. Noyes et al. 1984; Duncan et al. 1991), we rederived them following the procedure outlined in Maldonado et al. (2022) for TNG/HARPS-N spectra. That is, we first reobtained the S_{HK} index for our targets with HARPS-N spectra and converted them to the Mount Wilson scale using equation 3 of Maldonado et al. (2022).

During this process, we obtained the $(B - V)$ colours of the stars interpolating their effective temperatures in the updated tables of Pecauc & Mamajek (2013), which gives very similar results as using the $(B - V)$ -effective temperature relation provided by Maldonado et al. (2022) in their appendix A. Given that nine objects in our sample were observed by the TNG and LAMOST with its low-resolution spectrograph, we obtained a relation between the S_{HK} indexes obtained in Section 2.6 and the corresponding Mount Wilson S_{HK} values (see the Appendix).⁶ Using this relation we managed to derive R'_{HK} indexes for all stars observed by the low-resolution spectrograph of LAMOST, i.e. a total of 150 stars (27 observed by the TNG and 123 by LAMOST).

The logarithm of the R'_{HK} values above obtained for 70 stars (we do not apply any restriction regarding the errors) are represented as a function of their available rotational velocities (only values with errors of less than 1 km s^{-1}) in the bottom panel of Fig. 8. For comparison, we also include the measurements by Martínez-Arnáiz et al. (2010), Suárez Mascareño et al. (2015) and Maldonado et al. (2022). Note that Suárez Mascareño et al. (2015) do not provide rotational velocities but rotational periods (P), which we converted into velocities via $2\pi \times R/P$, where we adopted the radius (R) as given by the updated tables of Pecauc & Mamajek (2013) for the corresponding available spectral types. As it can be seen from the figure, our R'_{HK} values fall where they are expected for their rotational velocities. In the same way as for $L_{H\alpha}/L_{bol}$, we observe a saturation of $\log(R'_{HK})$ for fast rotators.

⁵This is always the case for the Ca II H&K lines, in which the radiated flux steadily increases with pressure.

⁶Only three objects with S_{HK} HARPS-N values had common observations with Mercator/HERMES, and none with Xinglong or LAMOST medium resolution spectrograph. As a consequence, we could not derive R'_{HK} for those stars observed with Mercator, Xinglong or LAMOST medium resolution.

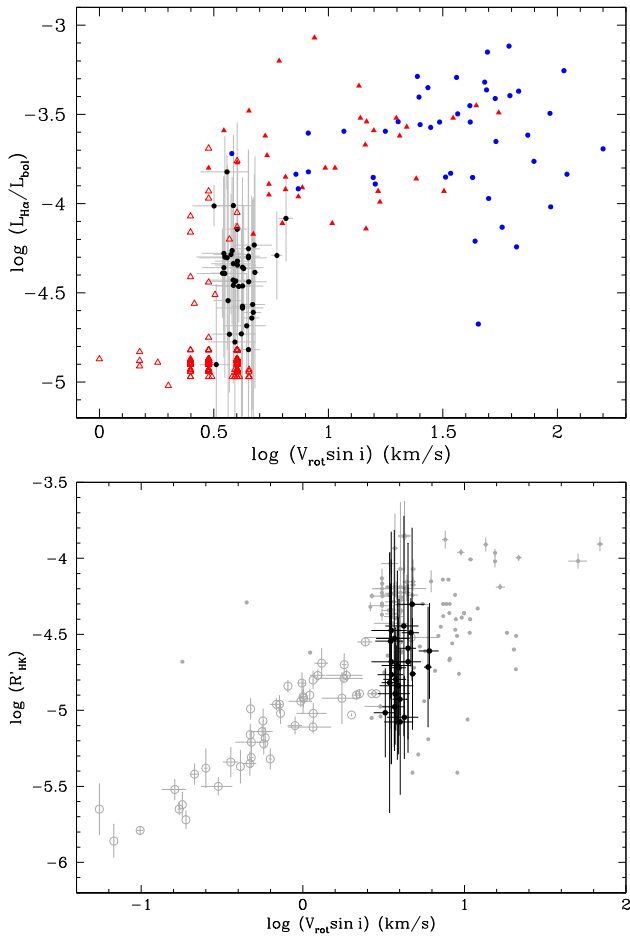


Figure 8. Top panel: $L_{H\alpha}/L_{bol}$ (indicating the strength of magnetic activity) as a function of projected rotation velocities for the 43 FGK stars considered in this work (black solid dots), the 47 M dwarfs in tight binaries with white dwarfs from Paper I (blue solid dots; note that in this case the rotational velocities are not affected by the $\sin i$ factor), and the 242 single M dwarfs from Reiners et al. (2012) (solid red triangles indicate accurately measured velocities, whilst open red triangles indicate upper limits). Bottom panel: $\log(R'_{HK})$ as a function of projected rotation velocities for 70 stars in our sample (black solid dots). Grey solid dots are data from Martínez-Arnáiz et al. (2010) (no errors provided since the authors do not report them) and Maldonado et al. (2022). Solid open circles are data from Suárez Mascareño et al. (2015) and represent rotational velocities not affected by the inclination factor.

5 THE AGE–ACTIVITY RELATION

The strength of magnetic activity – again represented quantitatively by $\log(L_{H\alpha}/L_{bol})$ and $\log(R'_{HK})$ – is illustrated as a function of age in Fig. 9. In the top panel of the figure, we considered main-sequence stars with errors in $\log(L_{H\alpha}/L_{bol})$ under 0.75 and age errors of less than 1 Gyr. This resulted in 87 FGK stars and 37 partially convective M dwarfs. In the middle panel, we show 43 stars (37 FGK and 6 partially convective M stars) with age errors of less than 1 Gyr and no error cuts applied to their $\log(R'_{HK})$ measurements.

Stars displaying $H\alpha$ in emission are shown as red open dots in the top panel of Fig. 9 and can mainly be seen at ages below 4 Gyr. The exceptions are J0531 + 2142 (5.5 ± 0.3 Gyr) and J1634 + 5710 (6.8 ± 0.4 Gyr). J1634 + 5710 is the hierarchical triple

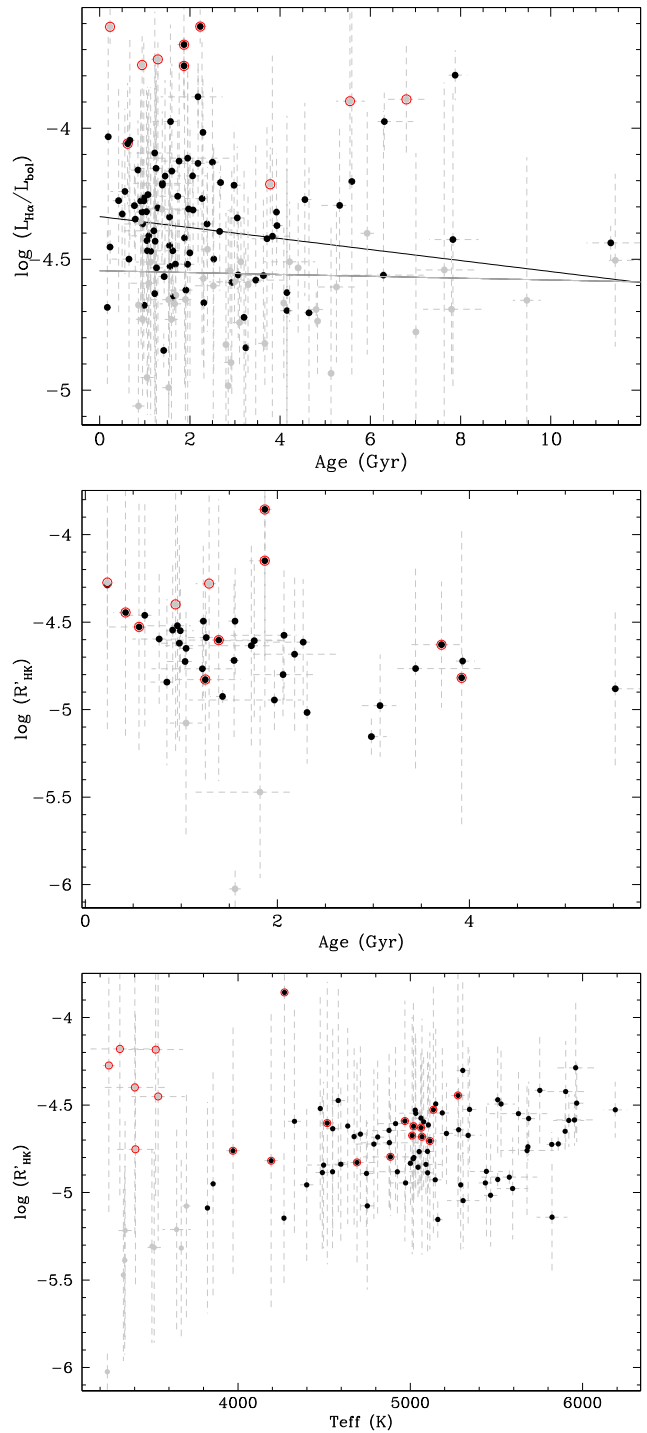


Figure 9. Top panel: $L_{H\alpha}/L_{bol}$ (indicating the strength of magnetic activity) as a function of age for the 87 FGK (black dots) and 37 partially convective M stars (grey dots) considered in this work. The solid black and grey lines are a linear fit to the FGK and M star data, respectively, which illustrate the tendency of M stars having lower values of $L_{H\alpha}/L_{bol}$. The red open circles indicate that $H\alpha$ in emission is visible in the spectra. Middle panel: $\log(R'_{HK})$ as a function of age for 37 FGK (black dots) and 6 partially convective M stars (grey dots) considered in this work. Bottom panel: $\log(R'_{HK})$ as a function of effective temperature for the entire sample of stars studied in this work (restricted to effective temperature errors of less than 200 K).

system composed of a DQ plus the short-period eclipsing binary CMDra. As mentioned earlier, in this case activity is due to the fast rotation induced by tidal locking. J0531 + 2142 has a current orbital projected separation of 1033 au; therefore, it is unlikely that wind accretion processes took place in the past. Given the lack of radial velocity measurements due to the broad H α emission, we suggest this system to be of similar nature as J1634 + 5710. The fact that most active stars are below 4 Gyr is in line with our results in Section 3, where we found null activity fractions for stars older than 5 Gyr (with the obvious exception of J1634 + 5710; see also Fig. 6). Moreover, the vast majority of the stars showing H α in emission have $\log(L_{H\alpha}/L_{bol}) > -4$, as expected. However, it is worth noting that 4 FGK stars with similarly high values of strength of magnetic activity do not show H α emission. As already discussed in the previous section, this is not entirely surprising since the H α absorption profile in FGK stars gradually decreases for increasing levels of magnetic activity, and only for the highest levels can it be seen in emission. This is generally not the case in M dwarfs, which have much weaker absorption profiles, and therefore are more prone to show emission once the level of magnetic activity increases. Thus, one would expect the $\log(L_{H\alpha}/L_{bol})$ values for M stars to remain roughly similar for inactive stars and to quickly rise for active stars, and to show a wider spread for FGK stars. Indeed, visual inspection of Fig. 9 shows a tendency for M stars to have lower $\log(L_{H\alpha}/L_{bol})$ values than FGK stars. This is confirmed by the linear fits to the data represented as black and grey solid lines for the FGK and M star data, respectively.

Further inspecting the top panel of Fig. 9 one can see that, apart from J1634 + 5710 and J0531 + 2142, one M star (J1043 + 5828) with an age of $\simeq 4$ Gyr and 3 FGK stars (J0707 + 2754, J0853 + 4406, and J1259 + 2528) with ages of $\simeq 2$ Gyr display H α in emission. The activity lifetimes of partially convective M stars are not expected to be higher than 2 Gyr and they are supposed to be even lower for FGK stars (West et al. 2008; Reiners & Mohanty 2012). J1043+5828 has a current projected orbital separation of 608 au, therefore magnetic activity could arise due to faster rotation induced by past episodes of wind accretion from the white dwarf precursor, when the separation was 2–5 times shorter. Regarding the three FGK stars, their current projected separations are 4500 au (J0707 + 2754), 6437 au (J0853 + 4406), and 2935 au (J1259 + 2528), which indicates wind accretion very likely did not take place in the past. We argue that the following physical mechanisms may result in these stars rotating faster than expected: (1) it is possible that some of them are suffering from weakened magnetic braking and, as a consequence, are anomalously rapid rotators (van Saders et al. 2016); (2) nearby hidden unresolved companions may exist that are massive enough for the stars in the inner binary of these plausible triple systems to be partially or totally tidally locked, thus increasing their rotation. Unfortunately, none of these stars have measured rotational nor radial velocities (except J1259 + 2528 with just one radial velocity value of -19.20 ± 1.80 km s $^{-1}$) to confirm or disprove these hypotheses. It is also plausible that the ages are not reliable for J1043 + 5828, J0707 + 2754 and J1259 + 2528, since no white dwarf spectral types are available and the evolutionary sequences employed might not be adequate if they are not DAs.

The middle panel of Fig. 9 shows a similar behaviour of $\log(R'_{HK})$ with age as $\log(L_{H\alpha}/L_{bol})$. That is, the $\log(R'_{HK})$ values are generally lower for partially convective M stars than for FGK stars. It is also important to mention that active M stars have $\log(R'_{HK})$ measurements considerably higher than inactive ones, whilst $\log(R'_{HK})$ is similar for both active and inactive FGK stars. This is further illustrated in the bottom panel of Fig. 9, where we represent $\log(R'_{HK})$ as a function

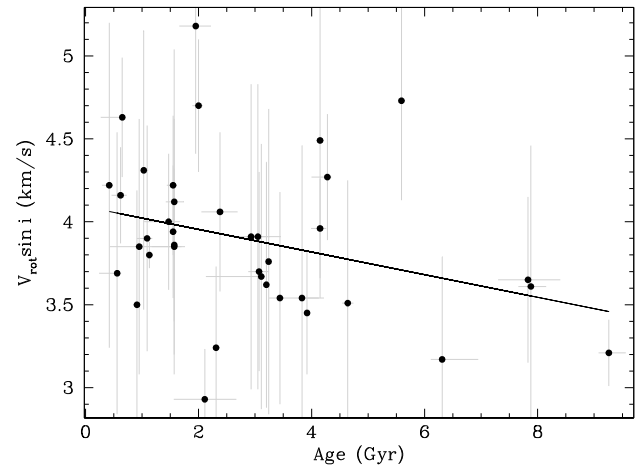


Figure 10. The projected rotational velocity as a function of age for 38 FGK stars. The solid black line is a linear fit to the data, which indicates the tendency of decreasing velocity with age.

of effective temperature for our entire sample (restricted to effective temperature errors of less than 200 K).

Finally, the middle panel of Fig. 9 also reveals four moderately old FGK stars (2–4 Gyr) which display Ca II H&K emission lines: J0221 + 5333, J0707 + 2754, J0853 + 4406, and J1743 + 1252. J0707 + 2754 and J0853 + 4406 also display H α in emission and have been discussed above. J0221 + 5333 and J1743 + 1252 both have two radial velocity measurements from spectra separated by 37 and 194 nights, respectively, and no variations have been detected. The current projected orbital separations are 333 au (J0221 + 5333) and 1482 au (J1743 + 1252), which indicates J0221 + 5333 might also be a candidate for spin-up rotation due to past wind accretion episodes. However, with a rotational velocity of 3.45 ± 0.37 km s $^{-1}$ this does not seem to be the case, unless the measurement is highly affected by the inclination factor.

6 THE AGE–ROTATION RELATION

We finally investigate the direct relation between age and rotation in this section. We considered all stars with projected rotational velocities associated with errors lower than 1 km s $^{-1}$ and age uncertainties under 1 Gyr, i.e. 38 FGK stars. The relation for these objects is illustrated in Fig. 10. None of them display H α nor Ca II in emission in their spectra, which is in line with the idea that slow rotators like those studied here ($V_{rot} \sin i \lesssim 10$ km s $^{-1}$) are inactive (or weakly active). Even though there seems to be a relatively large scatter of velocities at a given age, there is a tendency for decreasing the rotational velocity with age (represented by a linear fit to the data in Fig. 10). This confirms the expectations that rotation breaks with time, i.e. the so-called gyrochronology (e.g. Fouqué et al. 2023; Gaidos et al. 2023), and at the same time indicates that not all stars may suffer from weakened magnetic braking, since the oldest in our sample (>6 Gyr) are indeed among the ones with the lowest velocities.

7 CONCLUSIONS

Binary stars composed of a white dwarf and a main-sequence companion, WDMS binaries, are excellent tools for studying a wide variety of open problems in modern astronomy. In particular, deriving

reliable white dwarf ages makes them ideal objects for analysing age related relations such as the age–metallicity relation in the solar neighbourhood (Rebassa-Mansergas et al. 2016b, 2021), the age–velocity dispersion relation (Raddi et al. 2022) and, like in this work, the age–activity–rotation relation of low-mass main-sequence (FGKM) stars. Indeed, the results obtained in this work from a sample of WDMS binaries in CPMPs identified thanks to the *Gaia* astrometry and in our Paper I (Rebassa-Mansergas et al. 2013a) – from a sample of both close and wide binaries from the SDSS – have provided useful input for improving our understanding between the relation of age, magnetism, and rotation in low-mass stars.

We have shown that, with the exception of stars that are in close binaries (i.e. hierarquical triple systems composed of an inner binary plus an outer white dwarf), the activity fractions are null for stars older than 5 Gyr, independently of their effective temperatures, and that the rotational velocities tend to decrease with time. This confirms the idea that when stars grow old their level of magnetic activity decreases due to the effect of magnetic braking, which slows down their rotation. We have also found that the activity fractions for stars younger than 5 Gyr oscillate between $\simeq 10$ and 40 per cent. The low percentages obtained can be understood since the stars in our sample are either FGK or partially convective M stars, which are expected to have short activity lifetimes. However, it is worth noting that some stars in our sample are active despite being relatively old, in fact older than their expected activity lifetimes. We argue this indicates that a fraction of stars in our sample might suffer from weakened magnetic braking, they may have evolved through wind accretion episodes in the past or they are associated with unreliable ages due to the lack of white dwarf spectral types.

We have also evaluated how the strength of magnetic activity (studied via $L_{H\alpha}/L_{bol}$ and the R'_{HK} index) relates with both the projected rotational velocities and age. Given that our stars are slow rotators ($V_{rot} \sin i \lesssim 10 \text{ km s}^{-1}$) their measured values of $\log(L_{H\alpha}/L_{bol})$ and $\log(R'_{HK})$ fall in the expected region for inactive M stars or weakly active/inactive FGK stars, that is $-4 > \log(L_{H\alpha}/L_{bol})$, $(\log(R'_{HK}) > -5$.

Although the spread of $\log(L_{H\alpha}/L_{bol})$ and $\log(R'_{HK})$ values are nearly constant with age, they are found to be higher for FGK than for M stars. It is also worth mentioning that, as expected, the vast majority of stars displaying H α in emission are located above $\log(L_{H\alpha}/L_{bol}) = -4$. Partially convective and active M stars display also considerably higher $\log(R'_{HK})$ values than inactive ones. However, this is not generally the case for FGK stars, in which $\log(R'_{HK})$ is similar for both active and inactive stars.

Despite the fact that the SDSS WDMS sample we studied in Rebassa-Mansergas et al. (2013a) and the *Gaia* CPMPs studied in this work have been of fundamental importance, they come from very different surveys and the follow-up observations that we have performed were carried out using a wide variety of different telescopes and spectroscopic resolutions. As a consequence, not all our targets have measured H α fractional luminosities, R'_{HK} indexes, rotational velocities, effective temperatures, and ages. To solve this issue, the 4MOST (4 m Multi-Object Spectroscopic Telescope) project (de Jong et al. 2022), which will start operations in early 2024, will target, via its White Dwarf Binary Survey, $\simeq 2500$ FGKM main-sequence companions to white dwarfs in CPMPs and several thousand WDMS in tight orbits (Tolosa et al. 2023). Among the 2500 widely-separated binaries that 4MOST will observe, we expect $\simeq 10$ per cent to have total ages approximately equal to their cooling ages (i.e. negligible main-sequence lifetimes). This particular sample will be extremely useful in mitigating possible age uncertainties related to the initial-to-final mass relation. Moreover, all the main-

sequence stars will have available [Fe/H] values, which will avoid age uncertainties related to adopting a solar metallicity for the white dwarf precursors in those cases where the [Fe/H] is unknown. The fact that the white dwarfs in these CPMPs will also be observed by 4MOST will allow us to obtain a spectral type for each of them, thus avoiding unreliable ages due to wrong spectral type associations. Not only the considerably higher number of systems to be analysed, but also the observations to be carried out in an homogeneous way (thus ensuring the derivation of the same parameters for all stars) will allow us to investigate further and in a more robust way the relation between age, rotation, and activity in low-mass main-sequence stars.

ACKNOWLEDGEMENTS

This work has been partially supported by the (Spanish Ministerio de Asuntos Económicos y Transformación Digital) MINECO grant PID2020-117252GB-I00 and by the AGAUR/Generalitat de Catalunya grant SGR-386/2021. RR acknowledges support from Grant RYC2021-030837-I funded by MCIN/(Agencia Estatal de Investigación) AEI/10.13039/501100011033 and by ‘European Union NextGenerationEU/PRTR’. MEC acknowledges grant RYC2021-032721-I, funded by MCIN/AEI/10.13039/501100011033 and by the ‘European Union NextGenerationEU/PRTR’. MAH was supported by grant ST/V000853/1 from the Science and Technology Facilities Council (STFC). This project has received funding from the European Research Council (ERC) under the European Union’s Horizon 2020 research and innovation programme (grant agreement no. 101020057).

We thank the anonymous referee for the suggestions and comments that helped improving the quality of the paper.

We thank Dr. Xiang-Song Fang for sharing his relation of basal $EW_{H\alpha}$ versus effective temperature and his relation between effective temperature and $\chi_{H\alpha}$.

Based on observations made with the Telescopio Nazionale Galileo and Mercator Telescope awarded to the International Time Programme ITP18.8. Based on observations performed with the Xinglong 2.16 m telescope.

Guoshoujing Telescope (the Large Sky Area Multi-Object Fiber Spectroscopic Telescope LAMOST) is a National Major Scientific Project built by the Chinese Academy of Sciences. Funding for the project has been provided by the National Development and Reform Commission. LAMOST is operated and managed by the National Astronomical Observatories, Chinese Academy of Sciences.

This work has made use of data from the European Space Agency (ESA) mission *Gaia* (<https://www.cosmos.esa.int/gaia>), processed by the *Gaia* Data Processing and Analysis Consortium (DPAC; <https://www.cosmos.esa.int/web/gaia/dpac/consortium>). Funding for the DPAC has been provided by national institutions, in particular the institutions participating in the *Gaia* Multilateral Agreement.

DATA AVAILABILITY

The data underlying this article are available in the manuscript. Supplementary material will be shared on reasonable request to the corresponding author.

REFERENCES

- Althaus L. G., Camisassa M. E., Miller Bertolami M. M., Córscico A. H., García-Berro E., 2015, *A&A*, 576, A9
- Anguiano B., Freeman K. C., Steinmetz M., de Boer E. W., 2010, in Block D. L., Freeman K. C., Puerari I., eds, *Galaxies and their Masks*. p. 313

- Angus R., Aigrain S., Foreman-Mackey D., McQuillan A., 2015, *MNRAS*, 450, 1787
- Angus R. et al., 2019, *AJ*, 158, 173
- Angus R. et al., 2020, *AJ*, 160, 90
- Astudillo-Defru N., Delfosse X., Bonfils X., Forveille T., Lovis C., Rameau J., 2017, *A&A*, 600, A13
- Baliunas S. L. et al., 1995, *ApJ*, 438, 269
- Baraffe I., Chabrier G., 2018, *A&A*, 619, A177
- Barnes S. A., 2003, *ApJ*, 586, L145
- Barnes S. A., 2010, *ApJ*, 722, 222
- Barnes S. A., Kim Y.-C., 2010, *ApJ*, 721, 675
- Barnes J. R., Collier Cameron A., Donati J.-F., James D. J., Marsden S. C., Petit P., 2005, *MNRAS*, 357, L1
- Barrientos M., Chanamé J., 2021, *ApJ*, 923, 181
- Boffin H. M. J., 2015, in Boffin H. M. J., Carraro G., Beccari G., eds, *Astrophysics and Space Science Library* Vol. 413, p. 153
- Booth R. S., Poppenhaeger K., Watson C. A., Silva Aguirre V., Stello D., Bruntt H., 2020, *MNRAS*, 491, 455
- Bowler B. P. et al., 2021, *AJ*, 161, 106
- Browning M. K., 2008, *ApJ*, 676, 1262
- Browning M. K., Basri G., Marcy G. W., West A. A., Zhang J., 2010, *AJ*, 139, 504
- Camisassa M. E., Althaus L. G., Córscico A. H., Vinyoles N., Serenelli A. M., Isern J., Miller Bertolami M. M., García-Berro E., 2016, *ApJ*, 823, 158
- Camisassa M. E., Althaus L. G., Rohrmann R. D., García-Berro E., Torres S., Córscico A. H., Wachlin F. C., 2017, *ApJ*, 839, 11
- Camisassa M. E. et al., 2019, *A&A*, 625, A87
- Camisassa M., Torres S., Hollands M., Koester D., Raddi R., Althaus L. G., Rebassa-Mansergas A., 2023, *A&A*, 674, A213
- Capitanio L., Lallement R., Vergely J. L., Elyajouri M., Monreal-Ibero A., 2017, *A&A*, 606, A65
- Catalán S., Isern J., García-Berro E., Ribas I., 2008, *MNRAS*, 387, 1693
- Chabrier G., Küker M., 2006, *A&A*, 446, 1027
- Chaplin W. J. et al., 2014, *ApJS*, 210, 1
- Charbonneau P., 2005, *Living Rev. Sol. Phys.*, 2, 2
- Cui X.-Q. et al., 2012, *Res. Astron. Astrophys.*, 12, 1197
- Cummings J. D., Kalirai J. S., Tremblay P. E., Ramirez-Ruiz E., Choi J., 2018, *ApJ*, 866, 21
- de Jong R. S. et al., 2022, in Evans C. J., Bryant J. J., Motohara K., eds, *Proc. SPIE Conf. Ser. Vol. 12184*. SPIE, Bellingham, p. 1218414
- Donati J.-F. et al., 2008, *MNRAS*, 390, 545
- Dravins D., Lindegren L., Torkelsson U., 1990, *A&A*, 237, 137
- Dufour P., Blouin S., Coutu S., Fortin-Archambault M., Thibeault C., Bergeron P., Fontaine G., 2017, in Tremblay P. E., Gaensicke B., Marsh T., eds, *ASP Conf. Ser. Vol. 509*, 20th European White Dwarf Workshop. Astron. Soc. Pac., San Francisco, p. 3
- Duncan D. K. et al., 1991, *ApJS*, 76, 383
- Durney B. R., Stenflo J. O., 1972, *Ap&SS*, 15, 307
- Epstein C. R., Pinsonneault M. H., 2014, *ApJ*, 780, 159
- Fang X.-S., Zhao G., Zhao J.-K., Chen Y.-Q., Bharat Kumar Y., 2016, *MNRAS*, 463, 2494
- Fang X.-S., Zhao G., Zhao J.-K., Bharat Kumar Y., 2018, *MNRAS*, 476, 908
- Feiden G. A., Chaboyer B., 2014, *A&A*, 571, A70
- Fouesneau M., Rix H.-W., von Hippel T., Hogg D. W., Tian H., 2019, *ApJ*, 870, 9
- Fouqué P. et al., 2023, *A&A*, 672, A52
- Gaia Collaboration 2018, *A&A*, 616, A1
- Gaidos E., Claytor Z., Dungee R., Ali A., Feiden G. A., 2023, *MNRAS*, 520, 5283
- García R. A. et al., 2014, *A&A*, 572, A34
- García-Berro E., Torres S., Isern J., Salaris M., Córscico A. H., Althaus L. G., 2013, in *European Physical Journal Web of Conferences*. p. 05003
- García-Zamora E. M., Torres S., Rebassa-Mansergas A., 2023, preprint (arXiv:2308.07090)
- Garraffo C. et al., 2018, *ApJ*, 862, 90
- Gratton R. et al., 2021, *A&A*, 646, A61
- Gray D. F., 2008, *The Observation and Analysis of Stellar Photospheres*. Cambridge University Press, Cambridge, UK
- Gutiérrez Albarrán M. L. et al., 2020, *A&A*, 643, A71
- Hall J. C., Lockwood G. W., Skiff B. A., 2007, *AJ*, 133, 862
- Hall O. J. et al., 2021, *Nat. Astron.*, 5, 707
- Hartmann L. W., Noyes R. W., 1987, *ARA&A*, 25, 271
- Heintz T. M., Hermes J. J., El-Badry K., Walsh C., van Saders J. L., Fields C. E., Koester D., 2022, *ApJ*, 934, 148
- Houdebine E. R., Mullan D. J., Bercu B., Paletou F., Gebran M., 2017, *ApJ*, 837, 96
- Jeans J. H., 1924, *MNRAS*, 85, 2
- Jeffries R. D., Stevens I. R., 1996, *MNRAS*, 279, 180
- Jiménez-Esteban F. M., Torres S., Rebassa-Mansergas A., Cruz P., Murillo-Ojeda R., Solano E., Rodrigo C., Camisassa M. E., 2023, *MNRAS*, 518, 5106
- Kawaler S. D., 1988, *ApJ*, 333, 236
- Kimman R. et al., 2021, *AJ*, 161, 277
- Kraft R. P., 1967a, *ApJ*, 150, 551
- Kraft R. P., 1967b, *ApJ*, 150, 551
- Lacy C. H., 1977, *ApJ*, 218, 444
- Lallement R., Vergely J. L., Valette B., Puspitarini L., Eyer L., Casagrande L., 2014, *A&A*, 561, A91
- Lam M. C., Hambly N. C., Lodieu N., Blouin S., Harvey E. J., Smith R. J., Gálvez-Ortiz M. C., Zhang Z. H., 2020, *MNRAS*, 493, 6001
- Leighton R. B., 1969, *ApJ*, 156, 1
- Leiner E., Mathieu R. D., Gosnell N. M., Sills A., 2018, *ApJ*, 869, L29
- López-Sanjuan C. et al., 2022, *A&A*, 658, A79
- Lovis C. et al., 2011, preprint (arXiv:1107.5325)
- Magaudda E., Stelzer B., Covey K. R., Raetz S., Matt S. P., Scholz A., 2020, *A&A*, 638, A20
- Maldonado J., Martínez-Arnáiz R. M., Eiroa C., Montes D., Montesinos B., 2010, *A&A*, 521, A12
- Maldonado J. et al., 2022, *A&A*, 663, A142
- Mamajek E. E., Hillenbrand L. A., 2008, *ApJ*, 687, 1264
- Martínez-Arnáiz R., Maldonado J., Montes D., Eiroa C., Montesinos B., 2010, *A&A*, 520, A79
- McCleery J. et al., 2020, *MNRAS*, 499, 1890
- Meibom S., Barnes S. A., Platais I., Gilliland R. L., Latham D. W., Mathieu R. D., 2015, *Nature*, 517, 589
- Mestel L., 1984, in Baliunas S. L., Hartmann L., eds, *Lecture Notes in Physics*, Berlin Springer Verlag Vol. 193, Cool Stars, Stellar Systems, and the Sun. p. 49
- Mestel L., Spruit H. C., 1987, *MNRAS*, 226, 57
- Metcalfe T. S., Mathieu R. D., Latham D. W., Torres G., 1996, *ApJ*, 456, 356
- Metcalfe T. S. et al., 2012, *ApJ*, 748, L10
- Metcalfe T. S. et al., 2020, *ApJ*, 900, 154
- Miller Bertolami M. M., 2016, *A&A*, 588, A25
- Mittag M., Schmitt J. H. M. M., Schröder K. P., 2013, *A&A*, 549, A117
- Mohanty S., Basri G., Shu F., Allard F., Chabrier G., 2002, *ApJ*, 571, 469
- Morales J. C. et al., 2009, *ApJ*, 691, 1400
- Morgan D. P., West A. A., Garcés A., Catalán S., Dhital S., Fuchs M., Silvestri N. M., 2012, *AJ*, 144, 93
- Morin J. et al., 2008, *MNRAS*, 390, 567
- Morin J., Donati J.-F., Petit P., Delfosse X., Forveille T., Jardine M. M., 2010, *MNRAS*, 407, 2269
- Moss A. et al., 2022, *ApJ*, 929, 26
- Newton E. R., Irwin J., Charbonneau D., Berta-Thompson Z. K., Dittmann J. A., West A. A., 2016, *ApJ*, 821, 93
- Noyes R. W., Hartmann L. W., Baliunas S. L., Duncan D. K., Vaughan A. H., 1984, *ApJ*, 279, 763
- Pace G., 2013, *A&A*, 551, L8
- Parker E. N., 1955, *ApJ*, 122, 293
- Pecaut M. J., Mamajek E. E., 2013, *ApJS*, 208, 9
- Pietrinferni A., Cassisi S., Salaris M., Castelli F., 2004, *ApJ*, 612, 168
- Pineda J. S., Youngblood A., France K., 2021, *ApJ*, 918, 40
- Pipin V. V., Yokoi N., 2018, *ApJ*, 859, 18
- Pizzolato N., Maggio A., Micela G., Sciortino S., Ventura P., 2003, *A&A*, 397, 147
- Qiu D., Tian H.-J., Wang X.-D., Nie J.-L., von Hippel T., Liu G.-C., Fouesneau M., Rix H.-W., 2020, *ApJS*, 253, 58

Qiu D., Tian H.-J., Wang X.-D., Nie J.-L., von Hippel T., Liu G.-C., Fouesneau M., Rix H.-W., 2021, *ApJS*, 253, 58

Raddi R. et al., 2022, *A&A*, 658, A22

Raedler K.-H., Wiedemann E., Brandenburg A., Meinel R., Tuominen I., 1990, *A&A*, 239, 413

Rebassa-Mansergas A., Gänsicke B. T., Rodríguez-Gil P., Schreiber M. R., Koester D., 2007, *MNRAS*, 382, 1377

Rebassa-Mansergas A., Gänsicke B. T., Schreiber M. R., Koester D., Rodríguez-Gil P., 2010, *MNRAS*, 402, 620

Rebassa-Mansergas A., Nebot Gómez-Morán A., Schreiber M. R., Gänsicke B. T., Schwöpe A., Gallardo J., Koester D., 2012, *MNRAS*, 419, 806

Rebassa-Mansergas A., Schreiber M. R., Gänsicke B. T., 2013a, *MNRAS*, 429, 3570

Rebassa-Mansergas A., Agurto-Gangas C., Schreiber M. R., Gänsicke B. T., Koester D., 2013b, *MNRAS*, 433, 3398

Rebassa-Mansergas A., Ren J. J., Parsons S. G., Gänsicke B. T., Schreiber M. R., García-Berro E., Liu X.-W., Koester D., 2016a, *MNRAS*, 458, 3808

Rebassa-Mansergas A. et al., 2016b, *MNRAS*, 463, 1137

Rebassa-Mansergas A. et al., 2021, *MNRAS*, 505, 3165

Reiners A., Basri G., 2008, *ApJ*, 684, 1390

Reiners A., Basri G., 2009, *A&A*, 496, 787

Reiners A., Basri G., 2010, *ApJ*, 710, 924

Reiners A., Mohanty S., 2012, *ApJ*, 746, 43

Reiners A., Basri G., Browning M., 2009, *ApJ*, 692, 538

Reiners A., Joshi N., Goldman B., 2012, *AJ*, 143, 93

Renedo I., Althaus L. G., Miller Bertolami M. M., Romero A. D., Córscico A. H., Rohmann R. D., García-Berro E., 2010, *ApJ*, 717, 183

Réville V., Brun A. S., Matt S. P., Strugarek A., Pinto R. F., 2015, *ApJ*, 798, 116

Sadeghi Ardestani L., Guillot T., Morel P., 2017, *MNRAS*, 472, 2590

Schreiber M. R. et al., 2010, *A&A*, 513, L7

Shulyak D., Reiners A., Engeln A., Malo L., Yadav R., Morin J., Kochukhov O., 2017, *Nat. Astron.*, 1, 0184

Sills A., Pinsonneault M. H., Terndrup D. M., 2000, *ApJ*, 534, 335

Silva Aguirre V. et al., 2017, *ApJ*, 835, 173

Skinner J. N., Morgan D. P., West A. A., Lépine S., Thorstensen J. R., 2017, *AJ*, 154, 118

Skumanich A., 1972, *ApJ*, 171, 565

Soderblom D. R., 2010, *ARA&A*, 48, 581

Spiegel E. A., Zahn J.-P., 1992, *A&A*, 265, 106

Suárez Mascareño A., Rebolo R., González Hernández J. I., Esposito M., 2015, *MNRAS*, 452, 2745

Tolosa O. et al., 2023, *Messenger*, 190, 4

Torres S., García-Berro E., Althaus L. G., Camisassa M. E., 2015, *A&A*, 581, A90

Torres S. et al., 2023, *A&A*, 677, A159

Tuffs R. J., Popescu C. C., Völk H. J., Kylafis N. D., Dopita M. A., 2004, *A&A*, 419, 821

van Saders J. L., Ceillier T., Metcalfe T. S., Silva Aguirre V., Pinsonneault M. H., García R. A., Mathur S., Davies G. R., 2016, *Nature*, 529, 181

Vaughan A. H., Preston G. W., Wilson O. C., 1978, *PASP*, 90, 267

West A. A., Basri G., 2009, *ApJ*, 693, 1283

West A. A., Hawley S. L., Bochanski J. J., Covey K. R., Reid I. N., Dhital S., Hilton E. J., Masuda M., 2008, *AJ*, 135, 785

Wilson O. C., 1966, *ApJ*, 144, 695

Wilson O. C., 1968, *ApJ*, 153, 221

Wilson O. C., 1978, *ApJ*, 226, 379

Wright N. J., Newton E. R., Williams P. K. G., Drake J. J., Yadav R. K., 2018, *MNRAS*, 479, 2351

Yuxi, Lu Angus R., Curtis J. L., David T. J., Kiman R., 2021, *AJ*, 161, 189

Zhao J. K., Oswalt T. D., Rudkin M., Zhao G., Chen Y. Q., 2011, *AJ*, 141, 107

Zhao J.-K. et al., 2015, *Res. Astron. Astrophys.*, 15, 1282

Zorotovic M. et al., 2016, *MNRAS*, 457, 3867

Zurlo A. et al., 2013, *A&A*, 554, A21

SUPPORTING INFORMATION

Supplementary data are available at *MNRAS* online.

Table 1. In this table, we provide the number of WDMS binaries that are part of the full sample, and that are part of subsamples with available white dwarf total ages, with available main-sequence rotational velocities, with available main-sequence $H\alpha$ fractional luminosities and with available R'_{HK} indexes.

Please note: Oxford University Press is not responsible for the content or functionality of any supporting materials supplied by the authors. Any queries (other than missing material) should be directed to the corresponding author for the article.

APPENDIX: CONVERTING THE S_{HK} INDEX TO THE MOUNT WILSON SCALE

We obtained the S_{HK} index in the Mount Wilson scale of 27 stars that were observed with the HARPS-N spectrograph of the TNG using the routine developed by Maldonado et al. (2022, see Section 6). Nine of these stars were also observed by LAMOST with the low-resolution instrument. The S_{HK} indexes we obtained for these nine stars (Section 2.6) are compared to the corresponding values in the Mount Wilson scale in Fig. A1. A least squares fit to the data results in $S_{\text{HK,MW}} = (1.52 \pm 0.10) \times S_{\text{HK}} - (0.074 \pm 0.025)$. We used this equation to obtain the S_{HK} in the Mount Wilson scale of 123 additional stars observe by LAMOST with its low-resolution spectrograph.

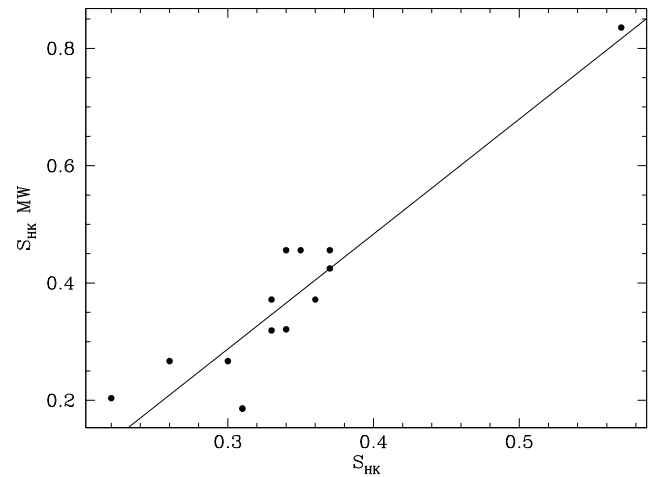


Figure A1. The S_{HK} index in the Mount Wilson scale as a function of the S_{HK} index directly measured by us for nine stars which have common TNG/HARPS-N and LAMOST low-resolution spectra.

This paper has been typeset from a $\text{\TeX}/\text{\LaTeX}$ file prepared by the author.